*J Mater Sci: Mater Electron* **(2023) 34:80**

# Defect driven enhanced ferromagnetism in Sb-modified $SnO_2$ nanoparticles

H. K. Mallick[1], Batakrushna Santara[2], M. P. K. Sahoo[1,*], and A. K. Pattanaik[1,*]

[1] *Department of Physics, Veer SurandraSai University of Technology, Burla, Odisha, India*
[2] *Department of Physics, Siddheswar College, Amarda Road, Balasore, Odisha, India*

**Received:** 2 July 2022
**Accepted:** 2 November 2022

## ABSTRACT

This work reports the tailoring of optical and magnetic properties in Sb-doped $SnO_2$ nanoparticles (NPs), i.e., $Sn_{1-x}Sb_xO_2$(x = 0.0, 0.03, 0.06, 0.09) synthesized by gel-combustion technique. The structural properties of these nanoparticles are investigated by the X-ray diffraction (XRD) technique. Detailed structural analysis shows the crystallization of all these NPs in tetragonal rutile structure, as observed in pristine $SnO_2$ without any trace of the secondary phase. Nevertheless, the incorporation of Sb dopant was found to increase the lattice constant systematically. Investigation of surface morphology by scanning electron microscopy and particle size by transmission electron microscopy also indicates a systematic increase in the grain size and particle size with Sb doping. Intriguingly, bandgap and room-temperature ferromagnetism (RTFM) are found to be sensitive to particle size and oxygen vacancies. UV–visible absorption, Fourier transform infrared, photoluminescence, and X-ray photoelectron spectroscopic measurements are carried out to explore the underlying physical mechanisms. Besides, the increase in RTFM and decrease in the bandgap witnessed in Sb-doped $SnO_2$ NPs can be exploited for magneto-optic and spintronic devices.

## 1 Introduction

Nanostructured tin dioxide ($SnO_2$) has been considered one of the most vital multifunctional materials displaying a diverse range of applications including in photocatalysis [1–4], gas sensors [5–9], Li-ion batteries [10–14], solar cells [15–18], optoelectronic devices [19–25], photothermal theragnosis agents [26, 27], spintronic devices [28, 29], and so on. The nanostructured $SnO_2$ exhibits unprecedented chemical, optical, electrical, superior magnetic properties, and excellent thermal stability, which are strongly influenced by shape and size effects, morphologies of the nanostructures, intrinsic defects, and dopants incorporation. Nonetheless, $SnO_2$ with intrinsic and extrinsic defects introduced through dopants is found to be crucial in enhancing the optical and magnetic properties as well as device performance.

---

Address correspondence to E-mail: mpksiit@gmail.com; akpattanaik_phy@vssut.ac.in

https://doi.org/10.1007/s10854-022-09437-6

The prominent intrinsic defects in $SnO_2$ nanostructures are oxygen vacancies (OVs) which form donor states inside the $SnO_2$ band gap, influencing its electronic structure and enhancing conductivity [30, 31]. Furthermore, the inclusion of OVs not only increases the absorption sites for the purpose of oxidization of gases, but also facilitates the gas sensing activity [32]. Besides, the formation of these OVs generates in-gap defect states of $SnO_2$ thereby reducing the band gap and extending the absorption to visible light which has a strong impact on the visible light photocatalytic activity, as well [33, 34], the OVs defect induced ferromagnetic ordering at room temperature in undoped $SnO_2$ nanostructures [35–38]. Moreover, suitable cation doping and the generation of intrinsic defects due to doping plays a pivotal role in enhancing the optical, electrical, and magnetic properties of $SnO_2$.

In recent decades, $SnO_2$-based nanostructures doped with special atoms into the host $SnO_2$ have garnered much attention for displaying enhanced optical and electronic properties. Among various dopants, Sb-doped $SnO_2$ has garnered much attention for its applications in gas sensors [39–41], solar cells [42], transparent electrodes for optoelectronic devices [43], smart windows for building energy management systems and automobiles [44], photothermal theragnosis agents [46, 47], and so on. Doping tin dioxide with electronic donors such as $Sb^{5+}$ yields a high conductivity without significant changes in its optical transmittance [45]. It has been demonstrated by Ponja et al. [45] that the doping of donors like $Sb^{5+}$ into $SnO_2$ generates OVs and accumulates these defects at the grain boundary. Such accumulation reduces the grain boundary barrier and improves electrical conductivity. So, as far as the band gap in Sb-modified $SnO_2$ is concerned, contradictory reports are found on the nature of the change in the band gap with doping of Sb. Some authors have reported an increase in band gap both experimentally [46–48], whereas some other experimental reports reveal a reduction in the band gap with Sb doping [49, 50]. Zhou et al. [51] demonstrate that strain induced decreased band gap in Sb-doped $SnO_2$ thin films. These reports suggest that dopant, particle size, and OVs played important role in tuning the band gap of Sb-doped $SnO_2$ nanostructures. More recently, Lv et al. [26] have reported a photothermal effect in Sb-doped $SnO_2$ with a conversion efficiency of 73.6%. It was demonstrated by these authors that the Sb-modified $SnO_2$ is beneficial in killing cancer cells and computed tomography (CT) imaging.

Various research groups [35, 52–59] reported the enhacement in ferromagnetic ordering in Ni, Co, Fe, Zn, Mn, Al-doped $SnO_2$ nanostructures due to an increase in OVs concentrations. However, excess doping leads to a reduction of magnetization in doped $SnO_2$ nanostructures [35, 60]. Some reports [60, 61] suggested structure-dependent magnetic relationship in which lattice contraction favors the ferromagnetic ordering, while lattice expansion decreases the ferromagnetism in $SnO_2$ nanostructures doped with Co and Fe. Using DFT calculations, Villamagua et al. [62] observed no magnetic moment in Zn-doped $SnO_2$ structure. Recently, Paraguay-Delgado et al. [57] demonstrated the $Zn_{Sn}$ defects-induced ferromagnetism in Zn-doped $SnO_2$, where the magnetic moment is localized at the surrounding oxygen atom instead of OVs. SaravanaKumar et al. [58] suggested that OVs alone cannot contribute to FM in Mn-doped $SnO_2$. Instead, exchange interaction between Mn and OVs enables such FM. On the other hand, Agrahari et al. [53] reported FM in undoped $SnO_2$ NPs, whereas Mn doping in it degrades the FM. The DFT calculation of Villamagua et al. [62] revealed that Sb-doped $SnO_2$ crystals cannot acquire magnetic moment, though the band gap width is decreased due to dopant incorporation. While Sb and Zn codoped $SnO_2$ crystal exhibit local magnetic moment, the Sb impurity contributes to the magnetic moment in the presence Zn impurity as Sb alone cannot induce any magnetic moment in the Sb-doped $SnO_2$ crystal [62]. These discussions indicate the inconsistency in the reports regarding the origin of ferromagnetism in doped $SnO_2$. Moreover, doping of Sb in $SnO_2$ results in a transparent conductive oxide (TCO) which exhibits high visible transmission. In addition, the nanoparticle of Sb-doped $SnO_2$ is suitable for Li-ion batteries, gas sensors, transparent electrodes, and electrochromic windows [20–24]. Though some studies report the optical and magnetic properties in Sb-doped $SnO_2$, however, these reports are highly inconsistent and contradictory. For instance, some authors have reported an increase in the band gap, whereas some other reports reveal a reduction in the band gap with Sb doping. Also, the reports on the origin of FM in Sb-doped $SnO_2$ are inconsistent. To the best of our knowledge, there are no experimental studies on the magnetic behavior of Sb-doped $SnO_2$ nanostructures so far.

This work reports the synthesis of Sb-doped $SnO_2$ Nanoparticles and studies the structural, morphological, optical, and magnetic properties of these samples. Since the defect plays a pivotal role in determining physical properties such as UV–Vis, PL, and magnetic properties, therefore, major emphasis has been given to understanding the influence of these defects in determining these outlined properties. Moreover, this work provides a design strategy to manipulate bandgap and improve optical and magnetic properties in $SnO_2$-based systems.

### 1.1 Experimental

Nanoparticles of Sb-modified $SnO_2$ with general formulae $Sn_{1-x}Sb_xO_2$ are prepared by the gel-combustion method. Here, the values of x are taken to be 0.0, 0.03, 0.06, and 0.09. High purity precursors of Sn-metal granules, $SbCl_3$, $HNO_3$, $C_6H_8O_7$, and $NH_4OH$ are taken for the synthesis of $Sn_{1-x}Sb_xO_2$ nanoparticles. At first, stoichiometric amounts of Sn-granules are dissolved in concentrated $HNO_3$ in a pyrex beaker by constant stirring. For Sb doping, $SbCl_3$ of the desired amount was added to the prepared solution during constant stirring. Further, citric acid is mixed with the above solution to further activate the reaction process. To maintain the pH value of the solution ~ 7, $NH_4OH$ was added dropwise. This process yields a transparent solution of a complex containing Sn–Sb–O-citric acid. It is to be noted that the pH adjustment in solution takes a vital role in the formation of the Sn–O/Sn–Sb–O and Citric acid complex. Moreover, in this step, the pH value of the solution was maintained to greater than 6.4. The prepared complex solution was slowly heated by maintaining a temperature of ~ 80 °C. The solution thus obtained was slowly condensed at 80–90 °C to transform the solution into a gel by eliminating leftover water. The obtained gel was further heated, auto-combustion started inside the gel, and gave desired powder. Finally, the obtained powder was ground and calcined at 750 °C to get the desired Sb-modified $SnO_2$ nanoparticles.

For the confirmation of room-temperature phase structure, XRD patterns were recorded by using Bruker Axs D8 diffractometer with Co Kα radiation and 2θ ranging from 20 to 80° with a step size of 0.02031°. The surface morphology of Sb-doped $SnO_2$ nanoparticles is recorded by using Sigma, Zeiss made scanning electron microscope (SEM) by depositing Au coating at the sample surface. The EDS spectra of the synthesized nanoparticles were done by using Oxford Instruments (UK) X-ray detector attached to SEM. The particle size of the Sb-doped $SnO_2$ nanoparticles was studied by using a Phillips Tecnai-12 transmission electron microscope (TEM). The Carry 5000 (Agilent Technology, USA) UV–VIS spectrometer was used to record the absorption spectra of the samples. For the study of PL (photoluminescence) properties, Horiba scientific fluoromax-4 was used. For the identification of chemical states and possible composition, XPS (X-ray photoelectron spectroscopy) spectra are recorded at room temperature using PHI 5000 Versa Prob II. FTIR spectra are recorded in a range of 500–4000 $cm^{-1}$ using Perkin Elmer, Spectrum BX. Magnetic hysteresis loops are recorded by using PPMS-VSM (Quantum Design, USA) with maximum applied magnetic field of ~ 10 kOe.

## 2 Results and discussion

### 2.1 Structural characterization

Figure 1a elucidates the room-temperature XRD patterns (open circles) of Sb-doped $SnO_2$ samples. The peaks and the intensity distribution of peaks resemble that of $SnO_2$ (JCPDS#41–1445). Secondary or impurity peaks are not observed from the XRD patterns indicating the formation of an Sb-doped sample in the desired phase. A systematic shifting of the peaks toward the lower Bragg angle is witnessed with Sb doping in pristine $SnO_2$, as shown in Fig. 1b. The general shifting of the XRD peaks toward the lower 2θ value is indicative of the expansion of the unit cell which can be explained as follows. The $Sn^{4+}$ ion in its 6-coordinated octahedral site has an ionic radius of 0.69 Å. Upon substitution of Sb ions at the $Sn^{4+}$ site will generate two possibilities owing to the multivalent states of Sb ions, i.e., $Sb^{3+}$ and $Sb^{5+}$. If $Sb^{3+}$ ions with ionic radii of 0.76 Å occupy the 6-coordinates $Sn^{4+}$ sites, then it will tend to expand the unit cell. However, if $Sb^{5+}$ ions with ionic radii of 0.6 Å occupy the 6-coordinates $Sn^{4+}$ sites, then this will lead to the contraction of the unit cell. Our XPS measurements (discussed later) confirm the presence of both these $Sb^{3+}$ and $Sb^{5+}$ ions in the doped sample. Thus, it can be presumed that though both the $Sb^{3+}$ and $Sb^{5+}$ ions are simultaneously present in the

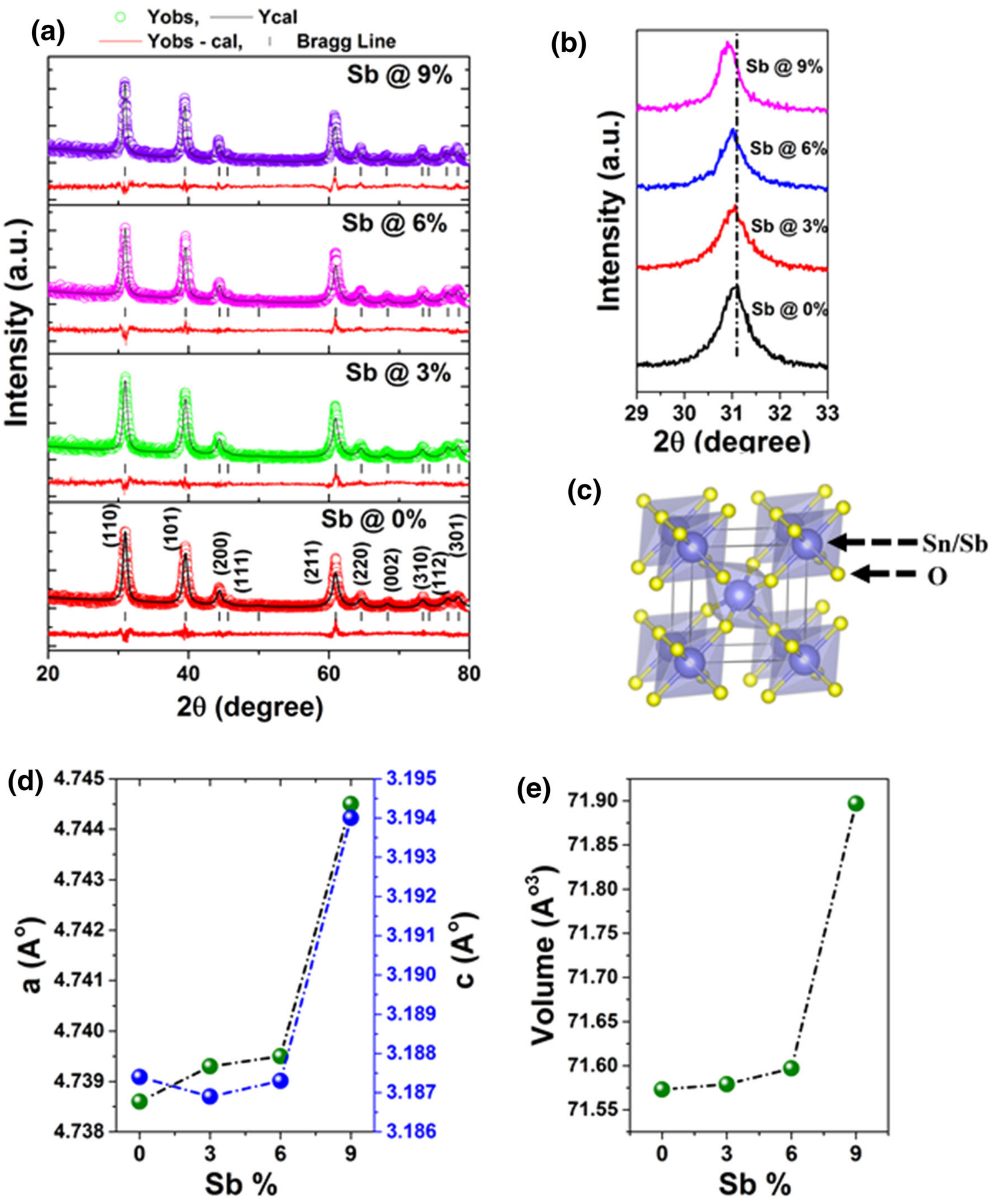

**Fig. 1** (**a**) Rietveld refined room-temperature XRD patterns of Sb-doped $SnO_2$ samples. (**b**) The magnified view of (1 1 0) Bragg peak. (**c**) Unit cell of $SnO_2$ obtained through Rietveld refinement. (**d**) Variation of lattice parameters a and c with Sb doping concentration. (**e**) The change in lattice volume

doped samples, quantitatively the $Sb^{5+}$ ions are outnumbered by $Sb^{3+}$ ions. Therefore, the effect of $Sb^{3+}$ ions dominates and thereby leading to a net expansion of the unit cell.

For the precise estimation of lattice parameters, and crystallite size, Rietveld refinement of room-temperature XRD patterns was carried out using Fullprof software. The parameters such as atomic position, site occupancy factor, and lattice parameters are taken into consideration. The background function is defined by 12 coefficient Fourier cosine series, and pseudo-Voigt function is used to acquire peak broadening parameters U, V, and W. Nevertheless, the instrumental contribution to the pattern has been corrected by using an instrumental resolution file. For pristine and Sb-doped samples, the Rietveld refinement was carried out in the rutile phase with space group P42/mnm. The refined lattice parameters and crystallite size are presented in Table 1. Figure 1c shows polyhedra of $SnO_2$ generated from the Rietveld refinement. Figure 1d, e illustrates the variation of lattice parameters and volume as a function of Sb concentration. It is observed that the lattice parameters and volume increase with an increase in the Sb content. Also, from Table 1, a systematic increase in crystallite size is observed with an increase in Sb content. A systematic increase in the crystallite size infers a direct dependency on the dopant concentration. Similar dopant concentration-dependent crystallite size variation has been observed for Sb-doped $SnO_2$ thin film [63].

## 2.2 Morphological studies

### 2.2.1 SEM imaging

Figure 2 illustrates the room-temperature SEM micrographs of Sb-doped $SnO_2$ NPs. All the samples exhibit a dense packing with roughly spherical shaped grains and without any pores. It is further observed that the grain size increases with an increase in the doping concentration. The average grain size obtained is 45 nm, 58 nm, 69 nm, and 85 nm for undoped, 3%, 6%, and 9% Sb-doped samples, respectively. Grain size may consist of more number of nanoparticles/crystallites. The adopted methodology of sample preparation for SEM imaging is that the samples are coated with gold prior to the observation of images to avoid the charging effect. Thus, there is the possibility of agglomeration of nanoparticles, and the average grain sizes observed in SEM are larger than the average crystallite sizes observed in XRD (listed in Table 1) in our samples as are mostly expected. The EDX spectrum (not shown) of undoped NPs reveals Sn and O elements, and doped samples show Sn, O, and Sb elements, indicating that no other contamination element was introduced during the sample preparation.

### 2.2.2 TEM imaging

The coating is avoided for TEM sample preparations, and the sample is well dispersed in DI water by ultrasonication and then drop casting on TEM grid, thus the agglomeration issue can be eliminated. Furthermore, TEM is preferred to analyze the size of nanoparticles of our samples owing to its higher resolution and to obtain microstructural information such as d-spacing and crystallinity. Figure 3 elucidates TEM micrographs of pristine and Sb-modified $SnO_2$ samples. From the micrographs, it is evident that both pristine $SnO_2$ and doped NPs are found to exhibit almost round-shaped morphologies. The average particle sizes, as presented in Table 1, systematically increase for doped samples which are consistent with the XRD and SEM results. Figure 3b–d shows the TEM images of 3%, 6%, and 9% Sb-doped NPs. It is important to note that the nanoparticle morphology is not affected by the Sb doping only except for a change in increase in the

**Table 1** Details of lattice parameters (a, c), particle sizes and band gaps (calculated from absorption spectra) of undoped and Sb-doped $SnO_2$ NPs

| Sb content in Sb:$SnO_2$ | Lattice parameters (Å) | | Unit cell volume (Å$^3$) | Crystallite size (nm) | Particle size (nm) from TEM | Bandgap (eV) |
|---|---|---|---|---|---|---|
| | a | c | a x a x c | | | |
| 0% | 4.7386 (2) | 3.1874 (1) | 71.573 | 9.7 | 9.88 ± 0.05 | 3.41 |
| 3% | 4.7393 (3) | 3.1869 (1) | 71.579 | 11.2 | 12.63 ± 0.03 | 3.38 |
| 6% | 4.7395 (4) | 3.1873 (2) | 71.597 | 13.5 | 14.75 ± 0.06 | 3.33 |
| 9% | 4.7445 (2) | 3.1940 (3) | 71.897 | 15.1 | 17.72 ± 0.02 | 3.25 |

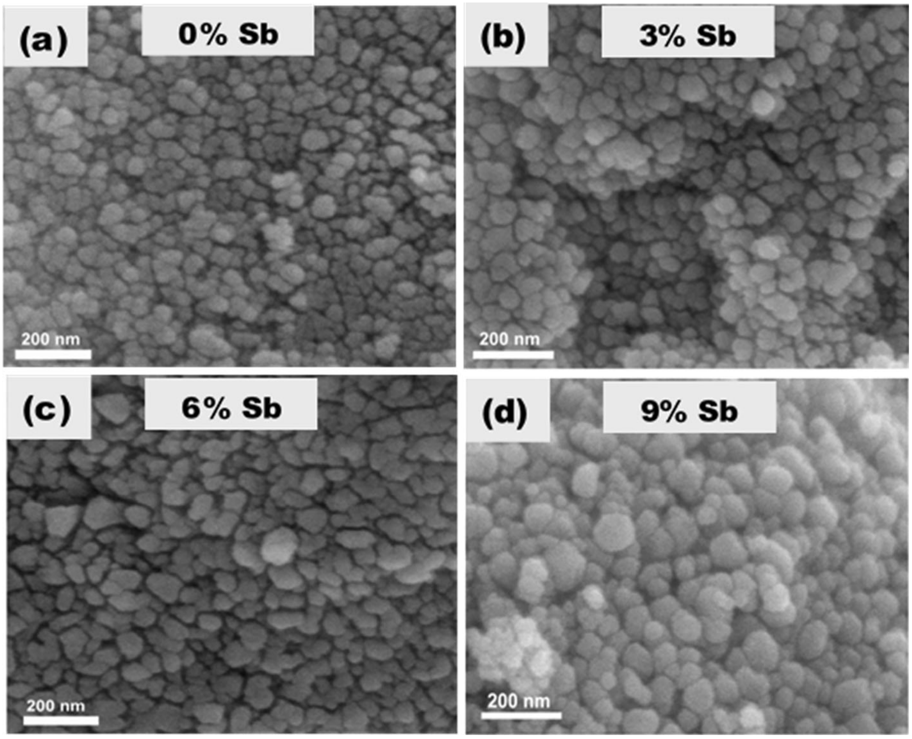

**Fig. 2** SEM images of the morphology of $SnO_2$samples: (**a**) undoped, (**b**) 3%Sb, (**c**) 6%Sband (**d**) 9% Sb

particle size. This suggests the successful incorporation of Sb into $SnO_2$ matrix and thus nullifies the possibility of any secondary or impurity phase. Figure 3 inset shows the selected area electron diffraction (SAED) pattern of corresponding undoped NPs indicating the polycrystalline nature of pristine and Sb-doped $SnO_2$ samples. Further, for reference, the diffraction rings are indexed as per the tetragonal rutile phase of $SnO_2$ (110), (101), (200), (211), and (301), as shown in Fig. 3b (inset). These SAED patterns also dictate that Sb is well incorporated into the $SnO_2$ crystal lattice. The high-resolution TEM (HRTEM) of the undoped sample is shown in Fig. 3b. The d-spacing of 0.332 nm corresponds to the (110) crystal plane of $SnO_2$, and the clear lattice fringe dictates that the as-grown NPs are highly crystalline. Figure 3e shows the lattice fringe of 6% doped NPs with d-spacing 0.334 nm corresponding to the (110) plane. The increase in d-spacing for the doped sample may be attributed to the incorporation of Sb atoms (larger ionic radii $Sb^{3+}$ ions) into the $SnO_2$ crystal lattice.

## 2.3 XPS studies

To explore the possible involvement of surface defects and understand the chemical environment in Sb-doped $SnO_2$ NPs, XPS has been used. The initial wide range XPS survey spectra (not shown) revealed no contamination and impurities other than dopant Sb in the as-grown undoped and Sb-doped $SnO_2$ NPs, respectively. Figure 4a–d illustrates the O 1 s spectra of the pristine-doped $SnO_2$ samples. The broadened O 1 s spectra at the higher binding energy side indicate the possible involvement of different oxygen species. To further shed light on the chemical states of oxygen in Sb-modified $SnO_2$, the asymmetric O 1 s peaks are deconvoluted. The deconvolution indicates the involvement of three peaks around 530.5, 531.5, and 532.3 eV. These peaks are due to the presence of lattice oxygen, Oxygen vacancies, and chemisorbed oxygen [56]. The asymmetric nature relatively increases with increasing dopants concentration. It can be noticed that the peak area of OVs significantly increases with increasing Sb doping, suggesting the systematic increase of OVs concentrations in $SnO_2$ with Sb doping concentrations. From enclosed the peaks, the concentration of oxygen vacancies is calculated to be 6.04%, 11.2%, 16.23%, and 22.8%, respectively. Figure 4e illustrates the Sn 3d spectra of pristine and Sb-doped $SnO_2$ samples. From these spectra, the presence of peaks at 486.6 and 495.05 eV confirms the Sn with $3d_{5/2}$ and $3d_{3/2}$ states indicating the $4+$ oxidation state of Sn in the

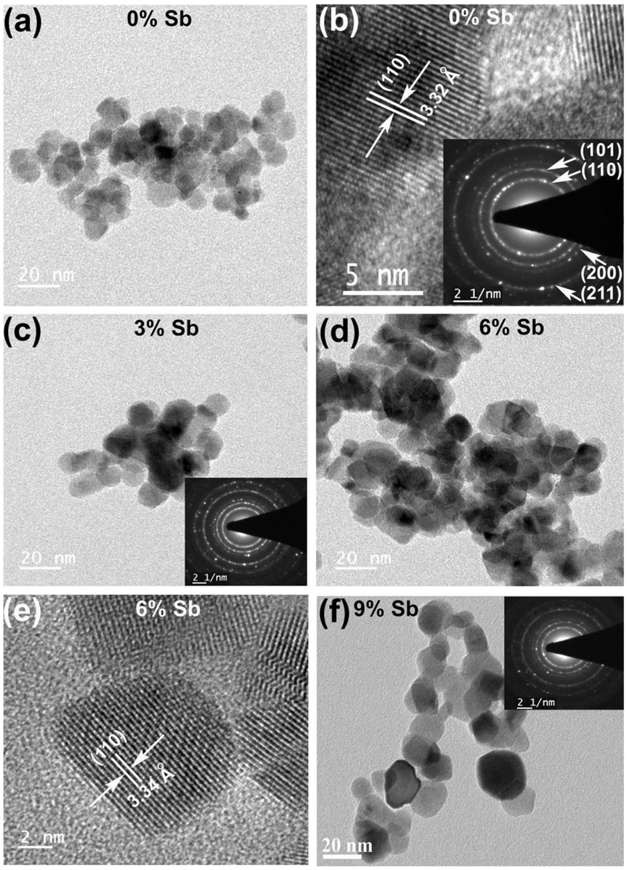

**Fig. 3** TEM image of$SnO_2$ samples doped with (**a**) 0%, (**c**) 3%Sb, (**d**) 6%Sb and (**f**) 9% Sb. The inset in each case shows the corresponding SAED pattern

synthesized samples. Upon increase in Sb doping concentration, a systematic shift of these peaks toward the lower binding energy side supports the successful incorporation of Sb into $SnO_2$ lattice and formation of OVs around Sn. Guan et al. [31] reported a similar low binding energy shift for N-doped $SnO_2$ NPs and suggested that the shift is due to the formation of OVs. Figure 4f shows the Sb 3d core level spectra of the doped samples. The Sb 3d spectrum consists of two characteristic peaks for $3d_{5/2}$ and $3d_{3/2}$, located at 530.5 and 539.90 eV, respectively, because of spin–orbit interactions [69]. The asymmetric nature of Sb 3d peaks suggests the presence of more than one oxidation state of Sb in the samples. Because of the overlapping of O 1 s and Sb $3d_{5/2}$ peaks, it is tough to analyze the accurate chemical state of antimony by fitting the Sb $3d_{5/2}$ peak. Thus, in order to investigate the oxidation state of Sb in the samples, the Sb $3d_{3/2}$ peaks of 6% and 9% doped samples were fitted into the two peaks (shown in Fig. 5a, b) centered at 539.89 and 541.21 eV corresponding to chemical states of $Sb^{3+}$ and $Sb^{5+}$, respectively [70]. From Fig. 5, it is noticed that almost all the Sb ions (about 92% in 6%Sb and 87% in 9%Sb-doped samples) are in the oxidation state + 3, which leads to a lattice expansion due to its much larger size compared with $Sn^{4+}$of the host lattice.

## 2.4 Optical absorption and PL studies

The particle sizes, OVs, and dopant may play important role in the optical properties of the synthesized pristine and doped $SnO_2$ NPs. Figure 6a shows the optical absorption spectra of Sb-modified $SnO_2$ NPs. A slight red-shift in the absorption edge has been noticed with Sb doping. This red-shift can be attributed to the OVs and/or size effect due to the incorporation of Sb dopant. For the estimation of the band gap, $(\alpha h\upsilon)^2$ is plotted against $h\upsilon$. This plot is known as Tauc plot and is shown in Fig. 6b. The band gap is calculated from the linear fits to the linear portion of the Tauc plot. The extrapolated lines fitted to the respective linear portions are shown in Fig. 6b. A systematic reduction in the band gap is noticed an increase in the Sb doping. The calculated band gaps are 3.41, 3.38, 3.33, and 3.25 eV for the pristine, 3%, 6%, and 9% doped samples, respectively. The decrease in the band gap can be correlated to the increase in crystallite size/grain size/ particle size with Sb doping, as is evident from XRD/SEM/TEM studies [64]. Besides, the OVs can also contribute to the band gap. In fact, the increase in oxygen vacancy may lead to decrease in the band gap [34]. Thus, the net reduction in band gap in Sb-doped $SnO_2$ can be ascribed to both the increase in NP sizes and OVs. Nevertheless, both XPS and PL (discussed later) studies confirm the presence of OVs in the pristine and doped samples. A similar reduction in the band gap has also been demonstrated by Yang et al. [34]. Note that the OVs concentrations increase (confirmed by XPS and PL studies) and the band gaps of doped samples decrease systematically with the increase in doping concentration. Generally, when a metal oxide is doped with impurities, its band gap reduces due to the introduction of either donor or acceptor levels into the original band gap [65]. Accordingly, the observed narrowing of the band gap in the doped samples may also be assigned to the doping of Sb within the $SnO_2$ host.

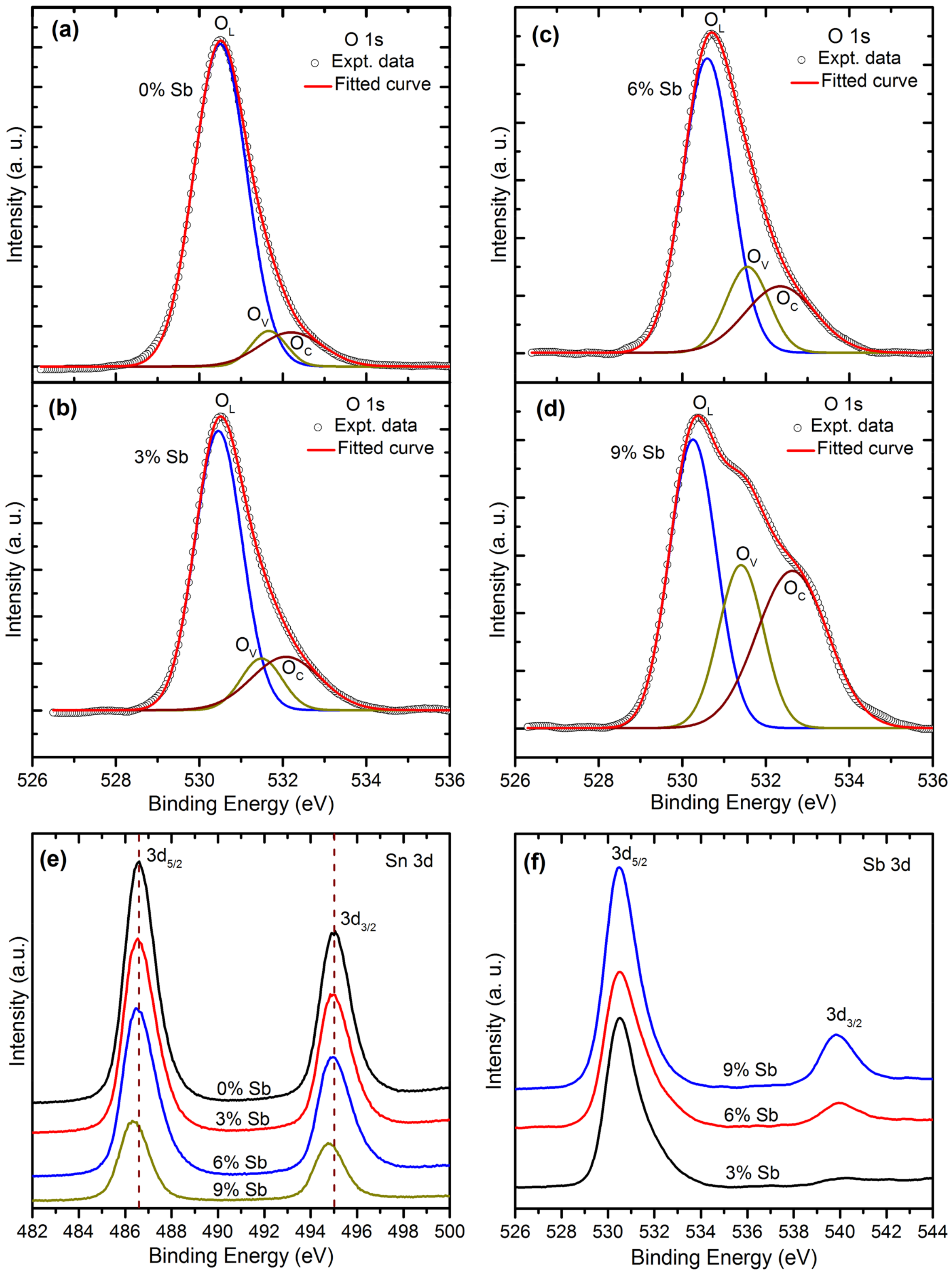

**Fig. 4** XPS spectra: O 1 s core level spectra of (**a**) undoped, (**b**) 3%Sb, (**c**) 6%Sb, and (**d**) 9%Sb-doped samples. The peaks are deconvoluted into three peaks showing the presence of three components; (**e**) Sn 3d core level spectra of undoped and Sb-doped $SnO_2$ NPs and (**f**) Sb3d spectra of doped samples

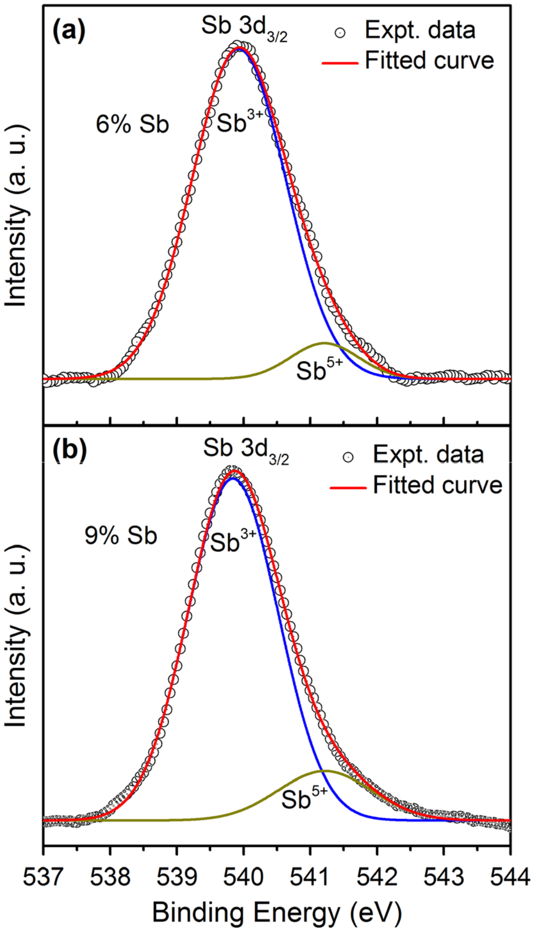

**Fig. 5** Deconvolution of Sb 3d$_{3/2}$ peak of XPS spectra of (**a**) 6% and (**b**) 9%Sb-doped samples, showing the presence of both Sb$^{3+}$ and Sb$^{5+}$ oxidation states in Sb-doped SnO$_2$ NPs

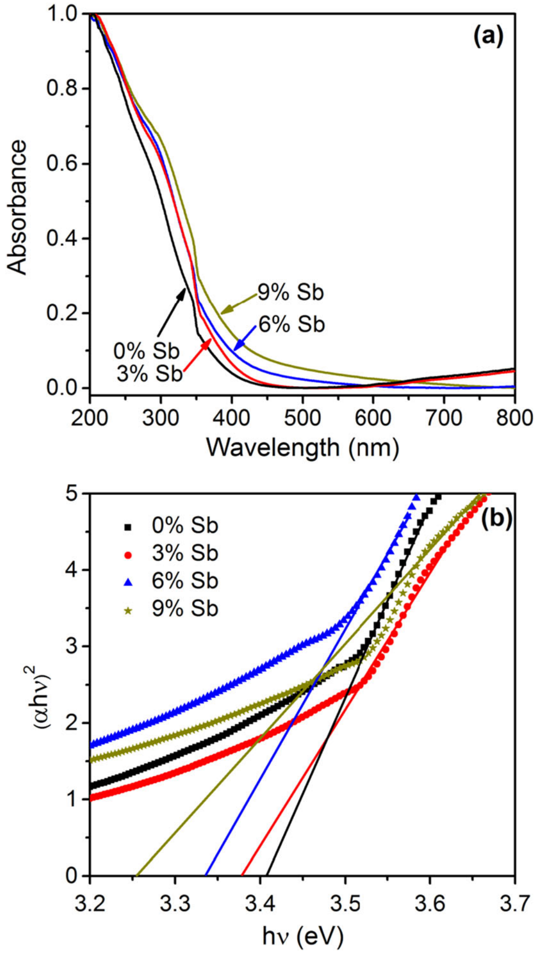

**Fig. 6** UV–Vis absorption spectra: (**a**) undoped, 3%Sb, 6%Sb and 9%Sb-doped SnO$_2$ NPs; (**b**) $(\alpha h\nu)^2 vs h\nu$ plot

Photoluminescence is an essential tool to explore defects and trap states associated with NP systems. Figure 7a elucidates the PL spectra of Sb-modified SnO$_2$ NPs, recorded at room temperature. The inset in Fig. 8a shows the PL spectrum of undoped SnO$_2$ NPs. Preliminary inspection of the PL spectra reveals an evolution of emission peaks with Sb doping, and all the doped samples are found to be significantly different from that of the undoped sample. However, all the spectra are found to be broadened indicating the possibility of more than one emission peaks. To explore the contributing emission peaks, the PL spectra are deconvoluted using Gaussian peaks, as shown in Fig. 7b, c. Pristine SnO$_2$involves three emission peaks centered on 367 nm, 436 nm, and 467 nm. Since the effective band gap of SnO$_2$ is 3.41 eV, therefore the first emission peak, i.e., 367 nm (3.38 eV) can be attributed to the NBE (near band edge emission) [66]. Peaks 436 nm (2.84 eV) and 467 nm (2.65 eV) can be correlated to the blue emission and transition between defect states oxygen vacancy (V$_o$) and singly ionized oxygen vacancy ($V_o^+$) [67]. In contrast to the pristine SnO$_2$, the Sb-doped SnO$_2$involves five emission peaks. The additional two peaks at 398 (3.12 eV) nm and 485 (2.56 eV) nm may be ascribed to the electron transition associated with the defect levels formed due to doping of Sb$^{5+}$ (donor state) and Sb$^{3+}$ (acceptor state), respectively [68]. It is worthwhile to note that Sb can have the ability to generate shallow donor or shallow acceptor states or both depending on its oxidation states. The Sb$^{5+}$ is considered a shallow donor when it replaces Sn$^{4+}$, whereas Sb$^{3+}$ considered as shallow acceptor when it replaces Sn$^{4+}$. Interestingly, XPS studies confirm the

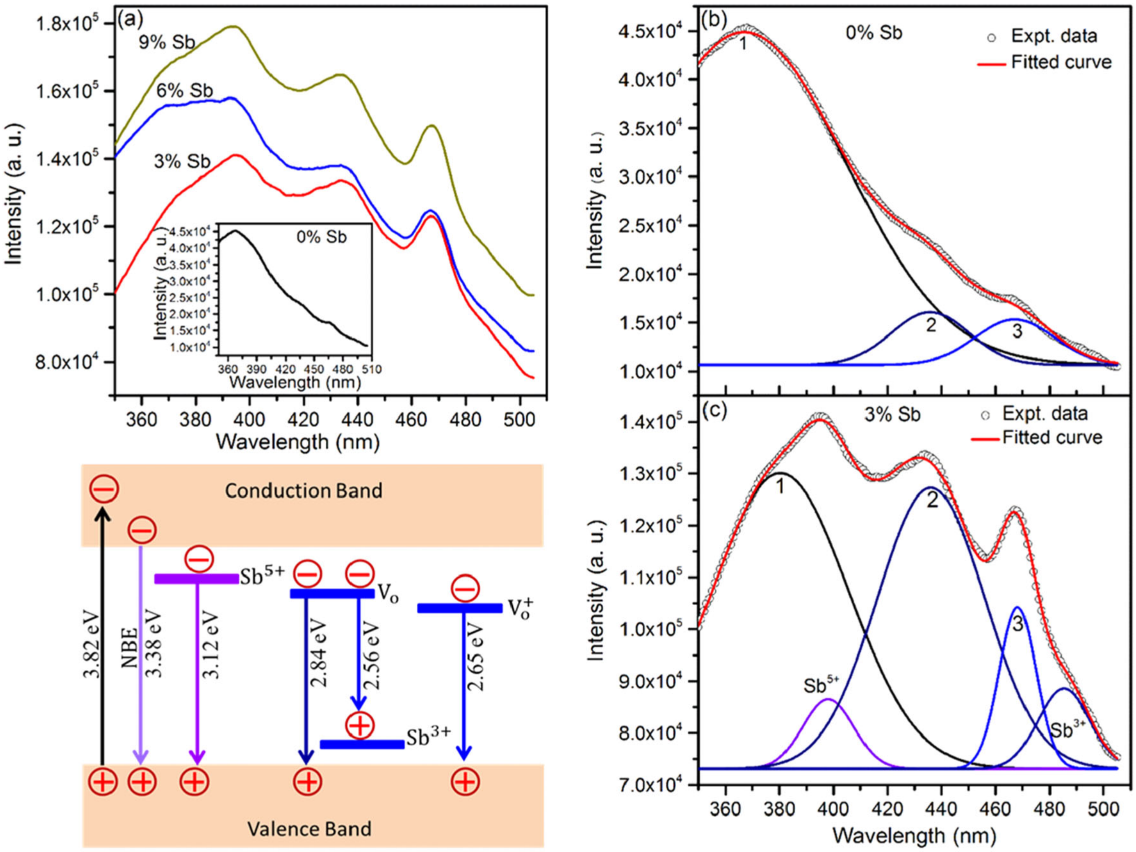

**Fig. 7** Room-temperature PL spectra for (**a**) Sb-doped $SnO_2$samples; inset is the undoped $SnO_2$ sample. Gaussian peak fitting of PL emission of (**b**) undoped and (**c**) 3%Sb-doped $SnO_2$ NPs; (**d**) Schematic diagram illustrating the physical origin of UV and visible PL emissions

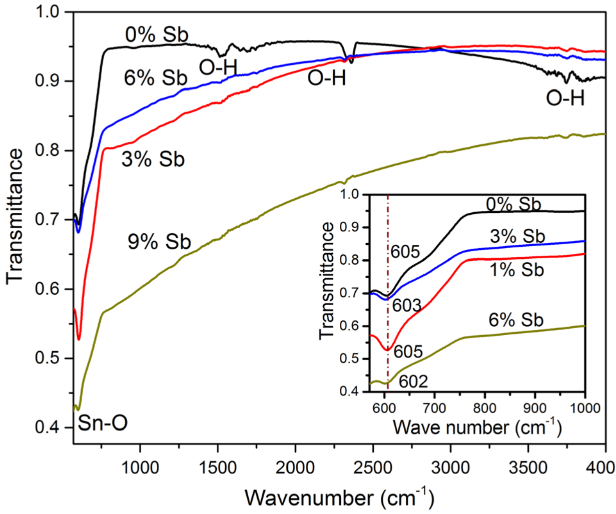

**Fig. 8** FTIR transmittance spectra of undoped and Sb-doped $SnO_2$ samples. The inset is the magnified view of Sn–O stretching mode

presence of both $Sb^{5+}$ and $Sb^{3+}$ states. Besides an unprecedented increase in PL intensities of 436 nm and 467 nm peak suggests a drastic increase in OVs concentration. Furthermore, a schematic band diagram is shown in Fig. 7 to explain the contributions of trap states to the PL spectrum. In general, the loss of O-atom from $SnO_2$ lattice generates $V_o$ along with an electron pair. The trapping of the electron at the $V_o$ can produce $V_o^+$. Moreover, these $V_o$ and $V_o^+$ form shallow and deep trap donor levels, respectively, within the band gap of $SnO_2$ and are associated with PL emission processes. The visible (blue) PL emission at 436 nm (2.84 eV) and 467 nm (2.65 eV) can be attributed to electron transition from $V_o$ and $V_o^+$ defect states to valence band, respectively. Emission peaks 398 (3.12 eV) and 485 (2.56 eV) reflect electron transition from the donor level formed by $Sb^{5+}$ to the valence band and donor level formed by $V_o$ to the acceptor level formed by $Sb^{3+}$.

## 2.5 FTIR studies

Figure 8 elucidates the FTIR spectra of pristine and Sb-doped $SnO_2$ nanoparticles. In general, the vibrational spectroscopic technique such as FTIR is employed to explore the impact of defects such as OVs/dopants on the vibrational modes in nanoparticles. The vibration mode at 605 cm$^{-1}$ is assigned to Sn–O stretching vibration of $SnO_2$ [71]. This peak position is slightly shifted to lower wave number with the increase in Sb doping. This type of shifting is attributed to the change in the bond length due to the replacement of heavier atoms such as Sb at relatively less heavy Sn atom site. This further confirms the successful substitution of Sn by Sb atoms in $SnO_2$ crystal lattice. The peaks appeared at 1521 cm$^{-1}$ and 2332 cm$^{-1}$ are related to the O–H bending and stretching vibrations due to the absorbed water on the surface when exposed to atmosphere [72]. The peak at 3745 cm$^{-1}$ is assigned to the stretching vibrations of O–H [72]. An additional peak observed at 2361 cm$^{-1}$in undoped sample may be assigned to atmospheric $CO_2$ molecules [72]. No other vibration except the characteristic modes of Sn–O proving the samples are free from impurities.

## 2.6 Magnetic studies and origin of ferromagnetism

Figure 9a illustrates the ferromagnetic hysteresis behavior of Sb-modified $SnO_2$ samples, recorded at room temperature. All samples exhibit non-saturating hysteresis loops. For pristine $SnO_2$, the maximum magnetization observed is 0.18 memu/g. Interestingly, with the increase in Sb doping, the maximum value of magnetization systematically increases. For 3%, 6%, and 9% Sb-doped $SnO_2$ samples, the maximum values of the magnetization observed are 0.19, 0.26, and 0.33 memu/g, respectively. A magnified view close to the origin is presented in the inset of Fig. 9a which shows the non-zero coercivity in all the samples.

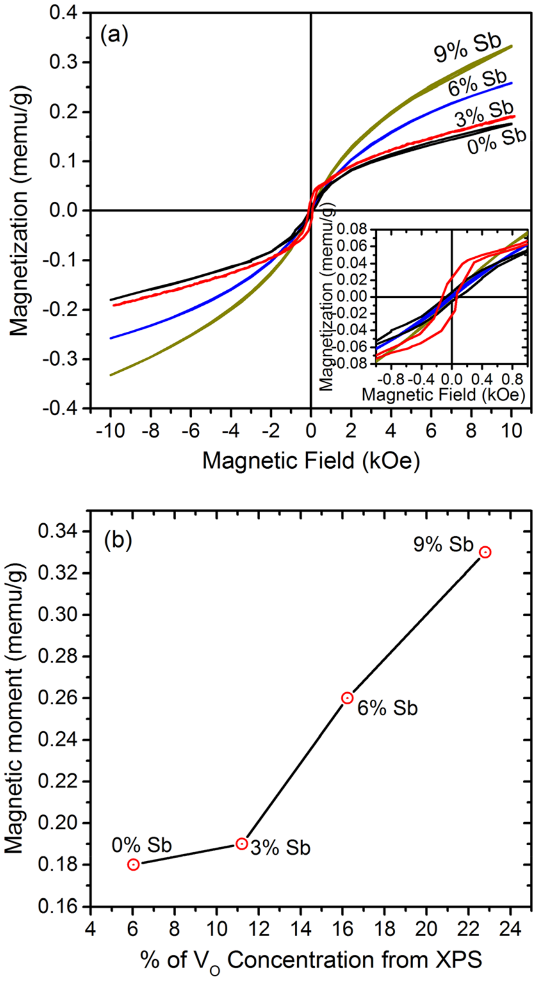

**Fig. 9** Room-temperature *M–H* loops Sb-doped samples, the inset shows a magnified view of *M-H* loops close to origin;(**b**) Plot of magnetic moment versus calculated oxygen vacancy concentrations from XPS analysis for undoped and doped samples

Though many authors have reported the existence of ferromagnetic like behavior in $SnO_2$, however, the physical origin of this behavior is still unclear. Some authors have suggested that the non-saturating magnetization in $SnO_2$ is due to the paramagnetic contribution of conduction electrons [73, 74]. Some authors suggested the contributions of oxygen and/or tin vacancies toward the observed magnetic moment [35–38, 52, 53]. Rahman et al. [52] suggested that Sn vacancy favors ferromagnetic ordering in undoped $SnO_2$, while several other reports [35–38, 53] strongly supported the $V_o$-induced FM in $SnO_2$ nanostructures. The first-principles calculations of Kılıç and Zunger [54] suggest that Sn vacancies have high formation energy and hence they are unlikely to be formed in $SnO_2$. Several OVs-related features such as narrowing of the optical band gap, visible PL emissions, and asymmetry of O 1S XPS in undoped and Sb-doped samples provide strong evidence that the observed FM in our undoped and doped $SnO_2$ NPs is induced by OVs defects. We observed strong visible PL intensities in doped samples compared to undoped sample which reveals the presence of more concentration of OVs in doped samples. From our

XPS results, it is observed that more concentration of surface OVs is associated with the doped samples. In this study, a coherence between increase in OVs concentration and magnetization is observed with Sb doping is witnessed. The one-to-one correlation between concentration of OVs and magnetic moment suggest that surface OVs are mainly responsible for the ferromagnetic ordering in our samples. The exact linear relationship between surface OVs and magnetic moments is not observed in our samples (Fig. 9b). However, the relationship between surface OVs and magnetic moments for doped samples is almost linear. Besides, the $V_o$ related defect environment with their proper distribution, the charge redistribution among the vacancies and/or dopants, and orbital overlapping/exchange interaction also play decisive role in bringing out magnetic behavior.

## 3 Summary

In summary, nanoparticles of Sb-modified $SnO_2$ are synthesized by a gel-combustion technique. Structural investigations reveal the crystallization of all the samples in tetragonal rutile phase. The SEM and TEM investigations explore an increase in grain size and particle size with the incorporation of Sb into $SnO_2$ host matrix. The investigation of band gap properties by UV–Vis spectroscopy suggests a decrease in the band gap. XPS investigations reveal the formation of doped Sb in both 5 + and 3 + oxidation states and an increase in the oxygen vacancy concentration with increase in Sb doping. The studies of magnetic hysteresis loop unfold a coherent increase in the maximum magnetization with Sb doping. The reduction in band gap and increase in the magnetic moment witnessed in the present work are attributed to the increase in particle size and oxygen vacancy concentration. The Sb modified with superior physical properties than its pristine counterpart can be exploited for spintronic applications and can stimulate the research community to explore new $SnO_2$-based nanoparticles with elemental doping.

## Author contributions

All authors contributed to the study's conception and design. Material preparation, data collection, and analysis were performed by HKM, BS, MPKS, and AKP. The first draft of the manuscript was written by HKM and all authors commented on previous versions of the manuscript. All authors read and approved the final manuscript.

## Funding

The authors declare that no funds, grants, or other support were received during the preparation of this manuscript.

## Data availability

The datasets generated during and/or analyzed during the current study are available from the corresponding author upon reasonable request.

## Declarations

**Competing interests** The authors have no relevant financial or non-financial interests to disclose.

**Ethical approval** There are no conflicts of interest. There is no involvement of Animals in current research work.

## References

1. M.A.H. Abdullah, S. Mika, B. Tanujjal, D. Joydeep, Appl. Surf. Sci. **370**, 229–236 (2016)
2. Morvarid Najjar, Hasan Ali Hosseini, Abdolhossen Masoudi, Zahra Sabouri, Asma Mostafapour, Mehrdad Khatami, Majid Darroudi, Optik Int. J. Light. Electron. Optics **242**, 167152 (2021)
3. S. Suthakaran, S. Dhanapandian, N. Krishnakumar, N. Ponpandian, J. Phys. Chem. Solids **141**, 109407 (2020)
4. A. Mamakhel, M. Søndergaard, K. Borup, Bo Brummerstedt Iversen. J. Supercrit Fluids. **166**, 105029 (2020)
5. P.G. Harrison, M.J. Willett, Nature **332**, 337–339 (1988)
6. S. Das, K.G. Girija, A.K. Debnath, R.K. Vatsa, J. Alloys Compd. **854**, 157276 (2021)
7. Myung Sik Choi, Jihye Ahn, Min Young Kim, Ali Mirzaei, Soon-Mok. Choi, Dong Won Chun, Changhyun Jin, Kyu Hyoung Lee, Appl. Surf. Sci **565**, 150493 (2021)
8. N.M. Shaalan, T. Yamazaki, T. Kikuta, Sens. Actuators B Chem. **166**, 671–677 (2012)

9. Mc.C. Rameech, S. Nozomi, S. Umesh, D. Soumen, K. Amit, J.C. Hyoung, K. Ramki, S. Sudipta, Nanoscale **4**, 7256–7265 (2012)
10. S. Wang, J. Liu, X. Yu, Y. Zhang, J. Liu, Z. Zhong, Z. Zhan, M. Zhang, X. Yang, P. Dong, Y. Zhang, Int. J. Electrochem. Sci. **14**, 9112–9121 (2019)
11. L. Na, S. Huawei, C. Hao, C.I. Wang, ElectrochimicaActa **130**, 670–678 (2014)
12. Hu. Zhiqing, Xu. Xinfeng, X. Wan, Yu. Kaifeng, Ce Liang. J. Alloys Compd. **835**, 155446 (2020)
13. Ruochen Zhang, Ke. Lia, Shouzhen Ren, Jiafu Chen, Xiaojian Feng, Yingqiao Jiang, Zhangxing He, Lei Dai, Ling Wang, Appl. Surf. Sci. **526**, 146685 (2020)
14. Kuiming Liu, Shengming Zhu, Xufeng Dong, Hao Huang, Min Qi, Adv. Mater. Interfaces. **7**, 1901916 (2020)
15. L. Zhengdao, Z. Yong, S. Ruzhong, X. Yan, X. Haiquan, Z. Zhigang, Chin. Sci. Bull. **59**, 2122–2134 (2014)
16. H.J. Snaith, C. Ducati, Nano Lett. **5**, 1259–1265 (2010)
17. Young Wook Noh, Ju Ho. Lee, In Su. Jin, Sang Hyun Park, Jae Woong Jung, Nano Energy. **65**, 104014 (2019)
18. Zhenxing Li, Rui Wang Jingjing. Xue, Xiaofei Xing, Yu. Chengcheng, Tianyi Huang, Junmei Chu, Kai-Li. Wang, Chong Dong, Zhiting Wei, Yepin Zhao, Zhao-Kui. Wang, Yang Yang, Am. Chem. Soc. **141**, 17610–17616 (2019)
19. S.H. Mohamed, J. Alloys Compd. **510**, 119–124 (2012)
20. J.M. Xu, L. Li, S. Wang, H.L. Ding, Y.X. Zhang, G.H. Li, CrystEngComm **15**, 3296–3300 (2013)
21. Y.D. Wang, I. Djerdj, B. Smarsly, M. Antonietti, Chem. Mater. **21**, 3202–3209 (2009)
22. J.M. Wu, Nanotechnology **21**, 235501 (2010)
23. U. Zum Felde, M. Haase, H. Weller, J. Phys. Chem. B **104**, 9388–9395 (2000)
24. J. Lim, B.Y. Jeong, H.G. Yoon, S.N. Lee, J. Kim, J. NanosciNanotechnol. **12**, 1675–1678 (2012)
25. H. Ohta, H. Hosono, Mater. Today **7**, 42 (2004)
26. Z. Lv, J. Li, F. Yang, K. Cao, Q. Bao, Y. Sun, J. Yuan, Front. Bioeng Biotechnol. **8**, 673 (2020)
27. N. Yu, C. Peng, Z. Wang, Z. Liu, B. Zhu, Z. Yi, M. Zhu, X. Liu, Z. Chen, Nanoscale **10**, 2542–2554 (2018)
28. G.A. Prinz, Science **282**, 1660 (1998)
29. S. Picozzi, Nat. Mater. **3**, 349 (2004)
30. W.J. Dong, J.J. Xu, C. Wang, Y. Lu, X.Y. Liu, X. Wang, X.T. Yuan, Z. Wang, T.Q. Lin, M.L. Sui, I.W. Chen, F.Q. Huang, Adv. Mater. **29**, 1700136 (2017)
31. X. Guan, P. Luo, X. Li, Y. Yu, D. Chen, L. Zhang, Int. J. Electrochem. Sci. **13**, 5667–5680 (2018)
32. M. Epifani, J.D. Prades, E. Comini, E. Pellicer, M. Avella, P. Siciliano, G. Faglia, A. Cirera, R. Scotti, F. Morazzoni, J.R. Morante, J. Phys. Chem. C **112**, 19540–19546 (2008)
33. L. Yang, Y. Yang, T. Liu, X. Ma, S.W. Lee, Y. Wang, New J. Chem. **42**, 15253–15262 (2018)
34. Y. Yang, Y. Wang, S. Yin, Appl. Surf. Sci. **420**, 399–406 (2017)
35. F.H. Aragón, J.A.H. Coaquira, P. Hidalgo, S.L.M. Brito, D. Gouvêa, R.H.R. Castro, J. Phys.: Condens. Matter. **22**, 496003 (2010)
36. H. Wang, Y. Yan, K. Li, X. Du, Z. Lan, H. Jin, Phys. Status Solidi B **247**, 444–448 (2010)
37. V.B. Kamble, S.V. Bhat, A.M. Umarji, J. Appl. Phys. **113**, 244307 (2013)
38. G.S. Chang, J. Forrest, E.Z. Kurmaev, A.N. Morozovska, M.D. Glinchuk, J.A. McLeod, A. Moewes, T.P. Surkova, N.H. Hong, Phys. Rev. B **85**, 165319 (2012)
39. Z. Wang, M. Zhi, M. Xu, C. Guo, Z. Man, Z. Zhang, Q. Li, Y. Lv, W. Zhao, J. Yan, C. Zhai, J. Mater. Sci. **56**, 7348–7356 (2021)
40. K. Suematsu, M. Sasaki, N. Ma, M. Yuasa, K. Shimanoe, ACS Sens. **1**, 913–920 (2016)
41. A.R. Babar, S.S. Shinde, A.V. Moholkar, C.H. Bhosale, J.H. Kim, K.Y. Rajpure, J. Alloys Compd. **509**, 3108–3115 (2011)
42. K. Balasubramanian, G. Venkatachari, Mater. Res. Express **6**, 1250k6 (2019)
43. M. Esro, S. Georgakopoulos, H. Lu, G. Vourlias, A. Krier, W.I. Milne, W.P. Gillin, G. Adamopoulos, J. Mater. Chem. C **4**, 3563–3570 (2016)
44. K.S. Cho, H.K. Kim, RSC Adv. **8**, 2599–2609 (2018)
45. S.D. Ponja, B.A.D. Williamson, S. Sathasivam, D.O. Scanlon, I.P. Parkin, C.J. Carmalt, J. Mater. Chem. C **6**, 7257–7266 (2018)
46. J.I. Scott, R.F. Martinez-Gazoni, M.W. Allen, R.J. Reeves, J. Appl. Phys. **126**, 135702 (2019)
47. A.R. Babar, S.S. Shinde, A.V. Moholkar, C.H. Bhosale, J.H. Kim, K.Y. Rajpure, J. Alloys Compd. **505**, 416–422 (2010)
48. Z.Q. Li, Y.L. Yin, X.D. Liu, L.Y. Li, H. Liu, Q.G. Song, J. Appl. Phys. **106**, 083701 (2009)
49. R. Medhi, C.H. Li, S.H. Lee, M.D. Marquez, A.J. Jacobson, T.C. Lee, T.R. Lee, A.C.S. Appl, Nano. Mater. **2**, 6554–6564 (2019)
50. T. Jintakosol, Appl. Mech. Mater. **749**, 141–145 (2015)
51. W. Zhou, Y. Liu, Y. Yang, P. Wu, J. Phys. Chem. C **118**, 6448–6453 (2014)
52. G. Rahman, V.M. García-Suárez, S.C. Hong, Phys. Rev. B **78**, 184404 (2008)
53. V. Agrahari, A.K. Tripathi, M.C. Mathpal, A.C. Pandey, S.K. Mishra, R.K. Shukla, A. Agarwal, J. Mater. Sci: Mater Electron. **26**, 9571–9582 (2015)
54. Ç. Kılıç, A. Zunger, Phys. Rev. Lett. **88**, 095501 (2002)
55. T. Zima, N. Bulina, Mater. Res. Bull. **117**, 48–55 (2019)
56. F. Xue, X. Liu, J. Liu, J. Phys. Chem. C **123**, 684–690 (2019)

57. F. Paraguay-Delgado, F.C. Vasquez, J.T. Holguín-Momaca, C.R. Santillán-Rodríguez, J.A. Matutes-Aquino, S.F. Olive-Méndez, J. Magn. Magn. Mater. **476**, 183–187 (2019)
58. M. Saravanakumar, S. Agilan, N. Muthukumarasamy, V. Rukkumani, A. Marusamy, A. Ranjith, Acta Phys. Pol. A **127**, 1656–1660 (2015)
59. H.K. Mallick, Y. Zhang, J. Pradhan, M.P.K. Sahoo, A.K. Pattanaik, J. Alloys Compd. **854**, 156067 (2021)
60. J. Hays, A. Punnoose, R. Baldner, M. Engelhard, J. Peloquin, K.M. Reddy, Phys. Rev. B **72**, 075203 (2005)
61. A. Punnoose, J. Hays, A. Thurber, M.H. Engelhard, R.K. Kukkadapu, C. Wang, V. Shutthanandan, S. Thevuthasan, Phys. Rev. B **72**, 054402 (2005)
62. L. Villamagua, R. Rivera, D. Castillo, M. Carini, AIP Adv. **7**, 105010 (2017)
63. E. Muhire, J. Yang, X. Huo, M. Gao, Mater. Sci. **25**, 21–27 (2019)
64. M.B. Sahana, C. Sudakar, G. Setzler, A. Dixit, J.S. Thakur, G. Lawes, R. Naik, V.M. Naik, P.P. Vaishnava, Appl. Phys. Lett. **93**, 231909 (2008)
65. N. Serpone, J. Phys. Chem. B **110**, 24287–24293 (2006)
66. B. Venugopal, B. Nandan, A. Ayyachamy, V. Balaji, S. Amirthapandian, B.K. Panigrahi, T. Paramasivam, RSC Adv. **4**, 6141–6150 (2014)
67. X. Wang, X. Wang, Q. Di, H. Zhao, B. Liang, J. Yang, Materials **10**, 1398 (2017)
68. A.R. Babar, S.S. Shinde, A.V. Moholkar, C.H. Bhosale, J.H. Kim, K.Y. Rajpure, J. Semicond. **32**, 053001 (2011)
69. S.M. Liu, W.Y. Ding, W.P. Chai, Phys. B Condens. Matter. **406**, 2303–2307 (2011)
70. S.G. Lee, S.B. Han, W.J. Lee, K.W. Park, Catalysts **10**, 866 (2020)
71. Y. Bouznit, A. Henni, Mater. Chem. Phys. **233**, 242–248 (2019)
72. V. Agrahari, M.C. Mathpal, S. Kumar, A. Agarwal, J. Mater. Sci: Mater Electron **27**, 3053–3064 (2016)
73. A. Sundaresan, R. Bhargvi, N. Rangarajan, U. Siddesh, C.N.R. Rao, Phys. Rev. B: Condens. Matter Mater. Phys. **74**, 161306(R) (2006)
74. B. Santara, P.K. Giri, K. Imakita, M. Fujii, Nanoscale **5**, 5476 (2013)